



Contributions of pore-throat size distribution to reservoir quality and fluid distribution from NMR and MIP in tight sandy conglomerate reservoirs

Meng Chen¹ · Jiakai Dai¹ · Xiangjun Liu¹ · Yan Kuang¹ · Minjun Qin² · Zhongtao Wang²

Received: 14 June 2018 / Accepted: 7 December 2018 / Published online: 28 December 2018
© Saudi Society for Geosciences 2018

Abstract

Overall pore-throat size distribution is a critical foundation for evaluating tight sandy conglomerate reservoirs. However, the pore-throat size cannot be easily obtained from a single technic due to the complex microstructure. In this paper, a new method was introduced to characterize the microstructure by combining thin sections, scanning electron microscopy (SEM), pressure-controlled injected mercury (PMI), rate-controlled injected mercury (RMI), and nuclear magnetic resonance (NMR). Twenty-four tight sandy conglomerate cores from the Baikouquan Formation of the Mabei oil field, northwest China, were selected to conduct the series of experiments. Overall pore-throat size distribution (TRD) was reconstructed by combining mercury injection porosimetry (MIP) with NMR with pores that were equivalent to triangular cross-section; the radii of the inscribed spheres were obtained to weaken the influence of irregular shapes by RMI. Irreducible water saturation of the cores was achieved by nitrogen displacement, which decreases with increasing of micropore proportion. An ideal relationship between permeability, movable water saturation, and micropore percentages was constructed which indicates the effect of microstructure on reservoir quality and fluid distribution in tight sandy conglomerate reservoirs.

Keywords Tight sandy conglomerate reservoirs · Mercury injection porosimetry · Nuclear magnetic resonance · Overall pore-throat size · Permeability · Fluid distribution

Introduction

With the expanding demands of energy throughout the world and progressively exhausted conventional oil reservoirs, the assessment of alternative supplementary energy sources such as tight oil has become increasingly important (Ghanizadeh et al. 2015; Chen et al. 2018a). Due to the complex microstructure and a significant portion of nanopores and throats of tight oil reservoirs, the natural productivity of a single well is usually lower than expected (Leng et al. 2015; Zhao et al. 2015). So, understanding the microstructure and its effect on petro-physical properties and the fluid distribution is essential

for evaluation and efficient exploitation in tight sandy conglomerate reservoirs (Clarkson et al. 2011).

Existing common techniques for microstructure analysis include scanning electron microscopy (SEM), thin-section analysis, X-ray computed tomography (CT), mercury injection porosimetry (MIP, including pressure-controlled mercury injection (PMI) and rate-controlled mercury injection (RMI)), nitrogen gas adsorption (N₂GA), and nuclear magnetic resonance (NMR) (Zhao et al. 2015; Xi et al. 2016). All these techniques have their advantages and disadvantages for characterizing microstructures in tight reservoirs. SEM and thin sections provide qualitative information such as deposition texture, diagenetic imprint, mineral composition, and partial pore-throat geometry, although the overall pore-throat information cannot be obtained from the technique (Neasham 1986; Klaver et al. 2012). Nano-CT can recognize the small pores between 50 and 600 nm but cannot identify pores smaller than 50 nm; also, it is uneconomical (Mayo et al. 2015; Kampschulte et al. 2016). N₂GA can only indicate a partial pore-throat size, such as 0.5~200 nm (Clarkson et al. 2013; Schmitt et al. 2013). PMI focuses more on throats, while large

✉ Meng Chen
chenmengyzu@163.com

¹ School of Geoscience and Technology, Southwest Petroleum University, Chengdu 610500, China

² Production Logging Center, China Petroleum Logging Co. Ltd., Xi'an 710200, China

pores might be missing and pores and throats cannot be separately recognized (Yao and Liu 2012; Clarkson et al. 2013). With RMI, mercury is injected at a constant velocity ($\sim 1 \times 10^{-6}$ mL/s) with the injected pressure and mercury volume recorded automatically. Then the pore-throat radius is calculated according to the Washburn equation (Washburn 1921), and the pore is equal to the radius of an isometric sphere (Yuan and Swanson 1989; Yuan 1991). The maximum intrusion pressure is 6.2 MPa (corresponding to the throat radius of 0.119 μm based on Washburn equation), and the smallest pores and throats identified by RMI seem to be larger than the true values in tight reservoirs. Then, an improved method combining RMI and PMI has been developed by Zhao et al. (2015) and Xiao et al. (2016a, b) with a modified capillary pressure curve, and pore-throat size distribution could be reconstructed. Although this method can increase the accuracy of the pore-throat size distribution estimation, there are still some limitations. First, the cross-sectional shapes of the pores and throats are always irregular triangles or polygons in tight reservoirs (Qiao et al. 2015; Zou 2017), so the pore radius calculated from equivalent spheres is obviously inaccurate. In addition, the pore radius frequency distribution by RMI is based on pore numbers, which differs from PMI (based on pore volumes corresponded to the injected mercury volume) with the pore-throat radius entirely calculated from the Washburn equation. As an effective and non-destructive technique, NMR can be used to indicate the overall pore-throat size (Yao et al. 2010; Jorand et al. 2011; Chen et al. 2018a). However, the measured data only indicate the transverse relaxation time (T_2) spectra but not the pore-throat radius; coefficients for converting from T_2 to corresponding pore-throat radius should be obtained to indicate a direct view (Volokitin et al. 2001; Xiao et al. 2012).

In this study, 24 tight sandy conglomerate cores from the Baikouquan Formation of the Mabei oil field, northwest China, were selected to conduct the thin-section, SEM, MIP, and NMR experiments. Pore-throat sizes determined by MIP were calibrated and correction coefficients between the NMR T_2 time and pore-throat radius that were also obtained. The overall pore-throat size distributions were reconstructed by combining MIP with NMR, and influences of pore-throat size on the fluid distribution and physical properties are then discussed.

Samples and experimental techniques

Twenty-four sandy conglomerate cylindrical rock core samples from the Triassic Baikouquan Formation of the Mabei oil field in the Junggar Basin were selected. Plugs 2.5 cm in diameter and 9 cm in length were cut into three parts, and the longer sections (approximately 5.0 cm) were machined into parallel faces and used for the NMR experiments; the

medium-length sections (approximately 2.0 cm) were used for PMI measurements, and the remainder was used for thin-section and SEM experiments. Meanwhile, six typical plugs from the 24 samples approximately 1.0 cm long were selected for RMI experiments.

Samples were carefully cleaned from oil by washing with methylbenzene and then dried at 105 °C for 48 h. Helium porosity varied between 3.99 and 16.41% and nitrogen permeability (measured at a confining pressure of 3 MPa using steady-state flow of nitrogen, and the Klinkenberg correction by a Core Lab CMSTM-300 automated permeameter) ranged from 0.009 to 70.980 mD. Then, the cores were saturated with a 13,000-ppm aqueous solution of CaCl_2 by immersion under vacuum (more than 48 h at 20 MPa) to ensure that the brine fully saturated the pore space. Low-field nuclear magnetic resonance core analysis unit (MesoMR23-060H-I, NIUMAG, China) was used to measure the T_2 spectra and the CPMG (Carr-Purcell-Meiboom-Gill) sequence was selected. The waiting time (T_w), echo time (T_E), echo number (NECH), and scanning number were set at 6000 ms, 0.301 ms, 18,000, and 32, respectively. After the T_2 spectra were measured under fully brine-saturated conditions, cores were displaced by nitrogen gas under a displacement pressure of 5.0 MPa until no more water was produced, and the T_2 spectra were also measured under the same setting parameters.

The high-pressure mercury injection experiment was conducted by a mercury porosimeter (Micrometrics AutoPore IV 9520, Micrometrics Inc., USA) by following the national standard of China (GB/T 29171-2012) with the maximum injection pressure was 200 MPa. A constant-rate mercury injection unit (ASPE-730, Coretest Systems Inc., USA) was employed to perform an experiment following the standard of the Daqing oil field in China (Q/SY DQ 1531-2012). The injection rate of mercury was $\sim 1 \times 10^{-6}$ mL/s and was terminated when the intrusion pressure reached the maximum of 900 psi (6.20 MPa). All the data were obtained automatically by software.

Theory

Correction of pore radius and distribution frequency for RMI

While by RMI, mercury is injected into the core samples at an extremely low rate as a non-wetting phase. The whole process could be divided into three steps which are Rison, Rheon, and Subison, corresponding to the injection pressure increasing and decreasing for mercury injected into minimum throats and wider pore bodies consecutively in the pore-throat system. The injected pressure will increase with the increasing injected mercury volume and terminate when the maximum pressure is reached

(Yuan and Swanson 1989; Yuan 1991). During RMI measurement, a single pore-throat system is composed of several Rheon and Subison processes following one Rison process (Fig. 1). A pore is considered as a sphere and the throat is considered as a cylinder as shown in Fig. 2a. Pore radii (R_p) are obtained based on the equivalent sphere, and the pore volume $V_p(i)$ is equal to the volume of injected mercury in the Subison process (Yuan and Swanson 1989). While in tight sandy conglomerate reservoirs, the pore cross-section is an irregular triangle or polygon as shown in Fig. 2b; the real pore radius R_o is equal to the radius of the inscribed sphere, and the radius must be overestimated based on the equivalent sphere. So there should be a relationship between the true and equivalent pore radii which could be represented as $R_o = \alpha R_p$ ($0 < \alpha < 1$), while the coefficient α is determined by the thin-section and SEM images.

Another important issue is that the pore and throat distributions by RMI corresponded to the number frequency with numbers equal to the Rheon or Subison, respectively. While by PMI, the pore-throat size distribution is the volume frequency corresponded to the injected mercury. Before the overall pore-throat size distribution curves are constructed, the number frequency by RMI must be converted to the volume frequency. PMI may reduce the number of large pore spaces due to the shielding effects of small pore spaces. RMI can characterize throats larger than $0.12 \mu\text{m}$ and pores larger than $40 \mu\text{m}$, so we mainly changed the pore radius distribution of RMI when constructing the TRD curves. The volume frequency distribution of the pore radius is based on the equivalent sphere theory, and the calculation models are shown in Eqs. (1) and (2):

$$V_{Shg}^p(i) = \frac{V_p(i)}{V} \times \sum V_{Shg}^p \tag{1}$$

$$V_p(i) = \frac{4\pi}{3} R_0^3(i) N_p(i) \tag{2}$$

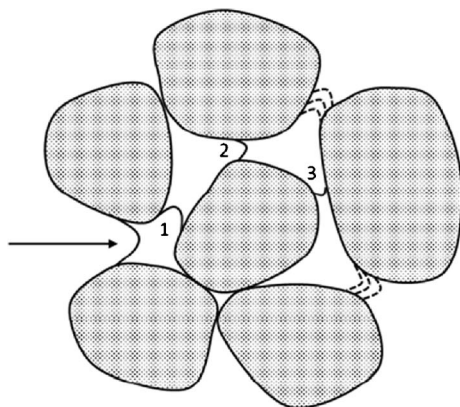


Fig. 1 Sketch of mercury injecting to pore space by RMI

where $V_{Shg}^p(i)$ is the volume percentage of the injected mercury in RMI, %; $V_p(i)$ is the pore volume at corrected pore radius, μm^3 ; $R_0(i)$ is the pore radius corrected by the equation $R_0 = \alpha R_p$, μm ; $N_p(i)$ is the number of pores at pore radius $R_0(i)$; V is the total pore volume calculated by the original pore radius, μm^3 ; and $\sum V_{Shg}^p$ is the total injected mercury saturation, %.

Pore-throat size distributions from T_2 spectrum by NMR

For NMR, the transverse relaxation time (T_2) is a combination of the bulk relaxation time (T_{2B} , ms), the diffusion relaxation time (T_{2D} , ms), and the surface relaxation time (T_{2S} , ms), which is defined as (Jorand et al. 2011; Timni et al. 2015; Wang et al. 2017),

$$\frac{1}{T_2} = \frac{1}{T_{2B}} + \frac{1}{T_{2S}} + \frac{1}{T_{2D}} = \frac{1}{T_{2B}} + \rho_2 \frac{S}{V} + \frac{D(\gamma GT_E)^2}{12} \tag{3}$$

where ρ_2 is the surface relaxivity, $\mu\text{m}/\text{ms}$; S/V is the pore surface/volume ratio, $1/\mu\text{m}$; D is the bulk-diffusion coefficient of the fluid present in the rock, $\mu\text{m}^2/\text{ms}$; γ is the gyromagnetic ratio, MHz/T ; G is the magnetic field gradient, $G/\mu\text{m}$; and T_E is the echo spacing time, ms. When T_{2B} is much larger than T_2 and T_E is sufficiently small, the first and third parts in Eq. (3) should be negligible. Meanwhile, S/V could be changed to r/F_r , where F_r is defined as the shape factor. Equation (3) can thus be converted to (Chen et al. 2018b),

$$T_2 = \frac{1}{\rho_2} \cdot \frac{V}{S} = \frac{1}{\rho_2 F_r} \cdot r \tag{4}$$

When the converted coefficient $C = 1/(\rho_2 F_r)$ is obtained, it can be determined as an experimental factor by combining the T_2 spectra with the PMI pore-throat radius distribution curves.

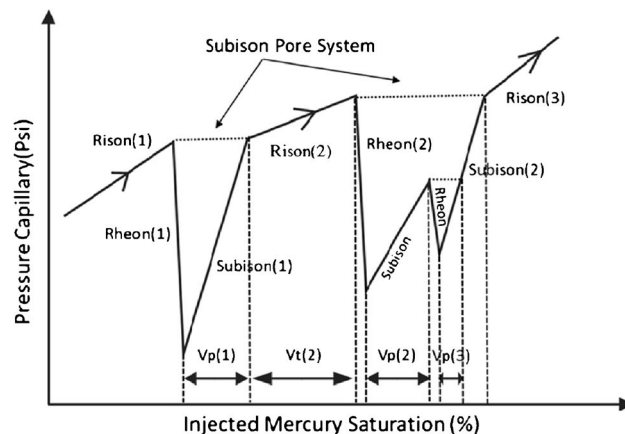
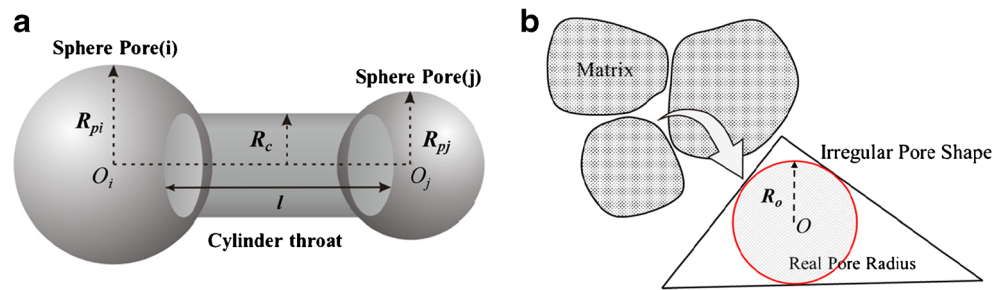


Fig. 2 **a** Calculation model of pore and throat in RMI. **b** Calculation model of pore radius in real reservoir



Results

Thin sections and SEM

Based on thin-section and SEM images (Fig. 3), pore spaces are identified and classified into four types, which are original intergranular pores, residual intergranular pores, grain dissolution pores, and microfractures. Due to the effects of compaction and cementation, the proportion of original intergranular pores is relatively low. The radii of those residual intergranular pores range from several to hundreds of micrometers. The grain dissolution pores are mainly dissolved from feldspar with a poor connectivity, and the maximum radius is less than the residual intergranular pores. The pore spaces decrease sharply and the physical properties become poor because of calcite cementation during later diagenesis. Microfractures are

formed during later diagenesis with no regularity, which are not widely developed (Fig. 3a, d).

Pressure-controlled mercury injection

To characterize the pore-throat size distribution in tight sandy conglomerate reservoirs, PMI for 24 plugs were measured and the mercury injection curves for seven typical samples were shown in Fig. 4a. Pore-throat radius was calculated according to Washburn’s equation, and the size distributions are plotted in Fig. 4b. From the shape of the mercury intrusion curves, core samples can be classified into three types. In type I (M139-3, FN10-23, and FN10-7), the displacement pressure P_d is lower than 0.3 MPa, which is corresponded to meso-macropores. The slope of the mercury intrusion curves increases sharply with the increase of injected mercury

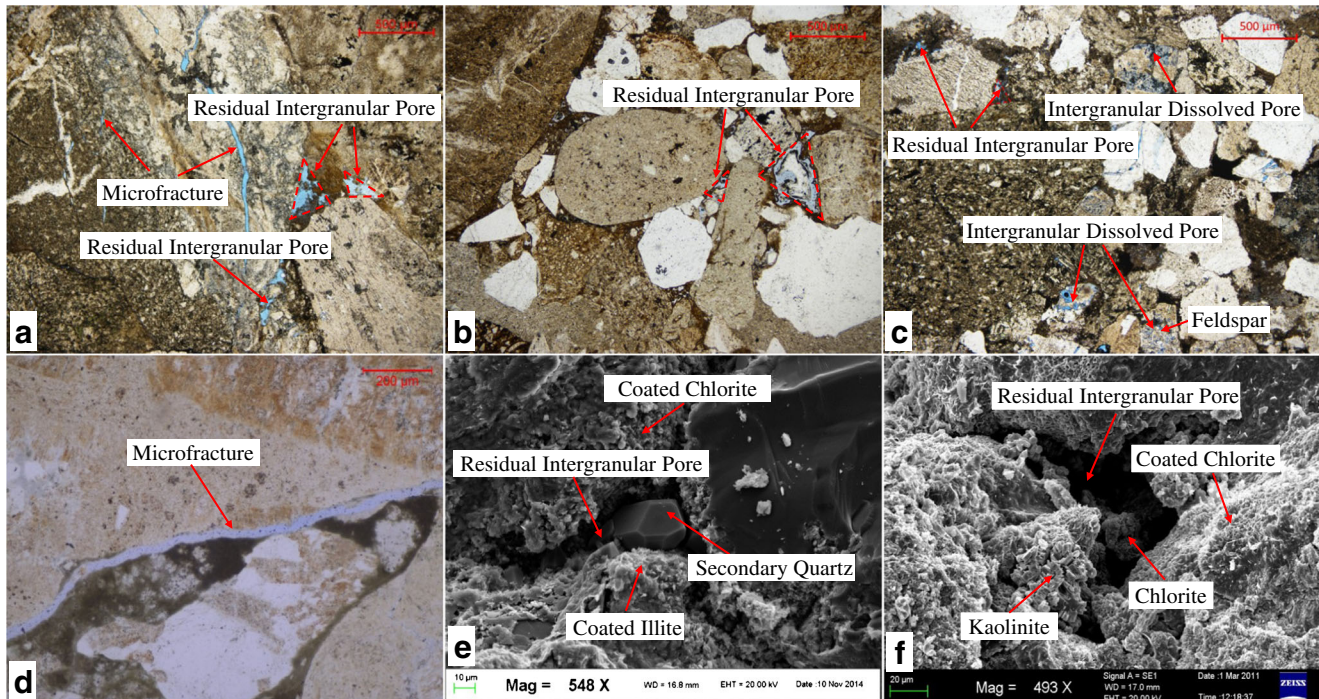


Fig. 3 The main pore types and pore shapes from SEM and thin-section images. **a** X723-4. The main pore types are residual intergranular pores and micro fractures. The pore shape is triangle. **b** M137-2. The main pore types are residual intergranular pores. The pore shape is triangle. **c** M152-6. The main pore types are residual intergranular pores and grain

dissolution pores. **d** X94-2. The main pore types are microfractures. **e** M137-1. The main pore type is the residual intergranular pore. The main clay minerals are chlorite and illite. **f** FN10-7. The main pore type is the residual intergranular pore. The main clay minerals are chlorite and kaolinite. The pore shape is triangle

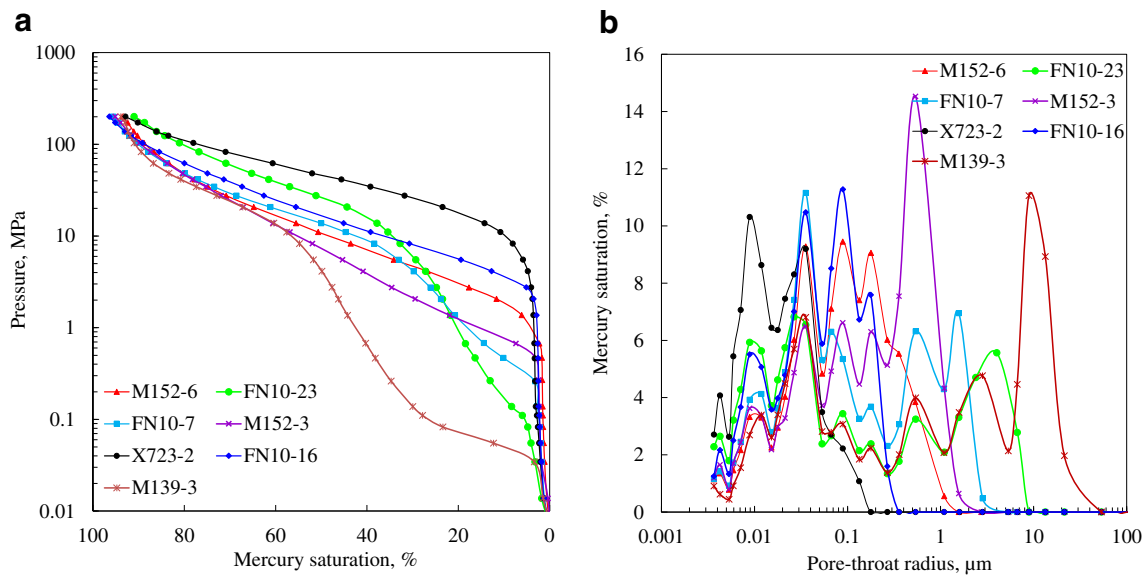


Fig. 4 a Mercury intrusion curves of PMI. b Pore-throat radii distribution curves calculated by Washburn equation

saturation, and the horizontal stage is short and not obvious. The pore-throat radius distribution curves show double peaks with one appears at the pore-throat radius between 0.01 and 0.1 μm and the other at the radius larger than 1.0 μm (Fig. 4b). In type II (M152-3 and M152-6), there is no horizontal stage with pore-throat radius ranges from 0.1 to 1 μm, and pores larger than 1 μm are not obvious. In type III (X723-2 and FN10-16), values of P_d are high and the pore-throat radii are smaller than 0.1 μm.

The parameters of the PMI experiment for 24 samples show that the average pore-throat radius (R_{ave}) ranges from 0.027 to 2.080 μm and mainly varies from 0.1 to 0.2 μm (Fig. 5a), while the maximum pore-throat radius (R_{max}) ranges from 0.13 to 21.37 μm and mostly varies from 1.0 to 2.0 μm (Fig. 5b). The pore-throat radius at the medium saturation (R_{mid}) is mainly found between 0.016 and 0.03 μm (Fig. 5c). The residual mercury saturation (S_{rHg}) mainly ranges from 38 to 46% and showed in Fig. 5d. The displacement pressure P_d mainly centers on

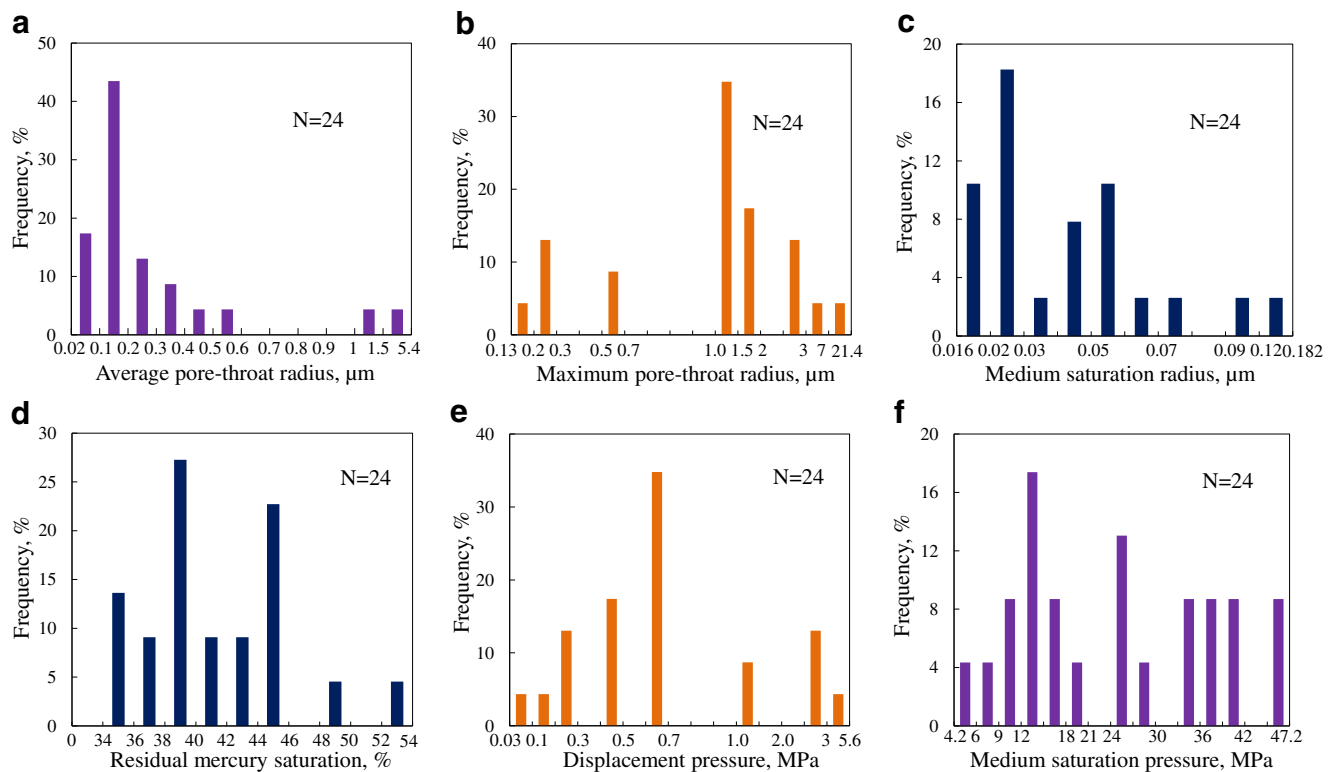


Fig. 5 a-f Parameters distribution of PMI experiment

0.65 MPa, and only small portions of samples are higher than 3.0 MPa (Fig. 5e), while the medium saturation pressure (P_{50}) ranges from 4.2 to 47.2 MPa with a non-uniform frequency distribution as shown in Fig. 5f. Those experimental parameters illustrate the complex and heterogeneous pore-throat sizes, and the pore-throat radius distribution indicates that micropore throats obviously develop in tight sandy conglomerate reservoirs. The sharp slopes of the mercury intrusion curves and high residual mercury saturation imply large discrepancies between pores and throats, and the flow characteristics are better with the increase of pore-throat radius.

The pore-throat radius of intergranular pores ranges from 30 to 40 μm in the thin-section images for sample FN10-7 (Fig. 3f). However, the measured maximum pore-throat radius by PMI is 2.83 μm in Fig. 4b, which is far lower than the radius in real reservoirs based on the intuitive observation. It means that macropores may be missed by PMI or just underestimated based on the Washburn's equation. Although it seems reasonable to characterize pores and throats smaller than 2.0 μm , the comparison indicates that the PMI method is unable to characterize the overall pore-throat distributions in tight sandy conglomerate reservoirs.

Rate-controlled mercury injection

The pore and throat distributions by RMI for six typical core samples are shown in Fig. 6; physical characteristic parameters (such as the pore and throat radii and the pore-throat ratio (defined as the radius ratio of pores to the connecting throats or the ratio of average pore radius to the average throat radius for a core sample)) for microstructure characterizing in tight sandy conglomerate reservoirs are also calculated and listed in Table 1. From RMI, it shows that pores range from 48 to 143 μm with peak values mainly around 73 μm , while throats mainly range from 0.2 to 1.2 μm with the pore-throat ratio varies from 105 to 760. There is no obvious difference in the pore size distributions and the peak values among those samples; meanwhile, the relationships between the physical properties and the pore radius are also unclear

(Fig. 6a). For throat size distributions in Fig. 6b and for the pore-throat ratio distributions in Fig. 6c, permeability k shows a clear relationship with them as k increases with the increasing of throat radius and decreasing of pore-throat ratio. This indicates that the size of the throat radius and the spatial correlation between the pores and throats are key factors controlling the permeability in tight sandy conglomerate reservoirs. However, RMI experiments mainly indicate throats larger than 0.12 μm and pores larger than 40 μm due to the limited maximum injection pressure while having a shortage for pores ranged from 5 to 40 μm . That means that RMI could be selected to complete the information of macropores lost by PMI.

Fluid distribution based on NMR

The fully brine-saturated T_2 spectra for 21 core samples were obtained and converted coefficients between the T_2 time and the corresponding pore-throat radius were calculated and ranged from 0.35 to 0.89 $\mu\text{m}/\text{ms}$ by combining the fully brine-saturated T_2 spectra with the pore-throat distributions by PMI based on the method proposed by Xiao et al. (2016a, b). The pore-throat radius distributions (Fig. 7a) and frequency histogram (Fig. 7d) of the pore-throat intervals by T_2 spectra for fully brine-saturated samples show that the pore radius ranges from 0.01 to 300 μm and mainly from 0.1 to 2 μm , indicating that micropores obviously develop in tight sandy conglomerate reservoirs. The converted T_2 spectra for bound water saturation (pore fluid displaced by nitrogen) were also obtained and plotted in Fig. 7b. It shows that areas of converted T_2 spectra for pores greater than 2 μm decrease sharply, and the fluid in pores larger than 50 μm is completely displaced, while areas with pores and throats smaller than 2 μm decrease slightly as there is little water is displaced. Bound water saturation of those tight core samples is high with values mainly range from 55 to 60% and shown in Fig. 7e. The movable fluid distributions are also obtained by subtracting the bound water from the fully brine-saturated T_2

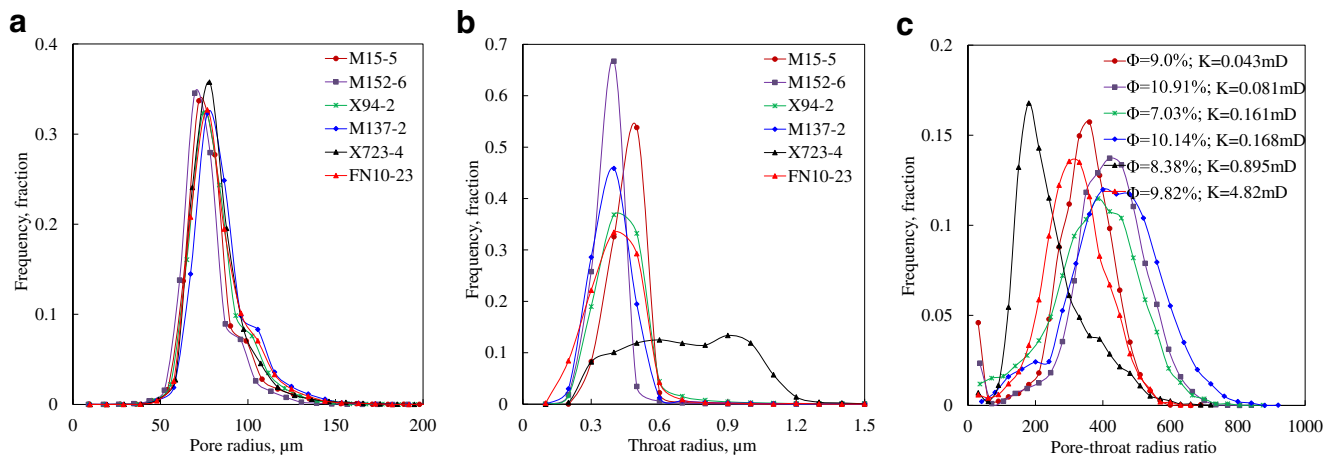


Fig. 6 **a** Pore size distribution from RMI. **b** Throat size distribution from RMI. **c** Pore-throat ratio distribution from RMI

Table 1 Physical parameters of the sample for RMI experiment and corresponding results

Sample	Depth (m)	ϕ (%)	k (mD)	R_t (μm)	R_p (μm)	η	S_p (%)	S_t (%)	S_f (%)	P_d (MPa)
M15-5	3091.02	9.00	0.04	2.27	127.71	319.95	27.16	21.12	48.27	1.58
M152-6	3124.56	10.91	0.08	1.81	125.95	397.19	20.14	15.95	36.09	1.89
X94-2	2841.72	7.03	0.16	0.67	127.07	357.74	29.10	15.09	44.19	1.38
M137-2	3255.18	10.14	0.17	0.37	128.53	413.45	32.43	17.66	50.09	1.54
X723-4	2682.26	8.38	0.90	1.26	121.02	230.99	49.68	22.24	71.91	0.59
FN10-23	2748.50	9.82	4.82	0.56	125.31	303.43	30.67	21.40	52.07	1.24

ϕ , porosity; k , permeability; R_t , average throat radius; R_p , average pore radius; η , pore-throat radius ratio; S_p , pore mercury saturation; S_t , throat mercury saturation; S_f , total mercury saturation; P_d , displacement pressure

spectra; it shows that movable fluid mainly ranges from 0.1 to 50 μm and the fluid in pore-throat radii less than 0.1 μm completely remained in Fig. 7c. Movable water saturation mainly ranges from 40 to 45%, and the frequency histogram for the 21 core samples is plotted in Fig. 7f.

As the pore-throat radius distributions by NMR range from 0.01 to 300 μm , which includes almost overall pores and throats in tight sandy conglomerate reservoirs. However, the distributions of micropores and throats less than 0.1 μm seem not accurate due to the graduation error and the precision of the experimental unit comparing with the PMI which has advantages in representing micropores and throats based on the large enough pressure for mercury injection. Meanwhile, RMI

can reflect the pores larger than 40 μm . So, a new TRD curve could be reconstructed by combining NMR T_2 spectra for fully brine-saturated samples with pressure-controlled injected mercury (PMI) and rate-controlled injected mercury (RMI).

Discussion

New TRD curve reconstruction

As the main type of pore section is triangular from SEM and thin-section images, the real pore space could be equivalent to a regular tetrahedron and the pore radius equal to the radius of

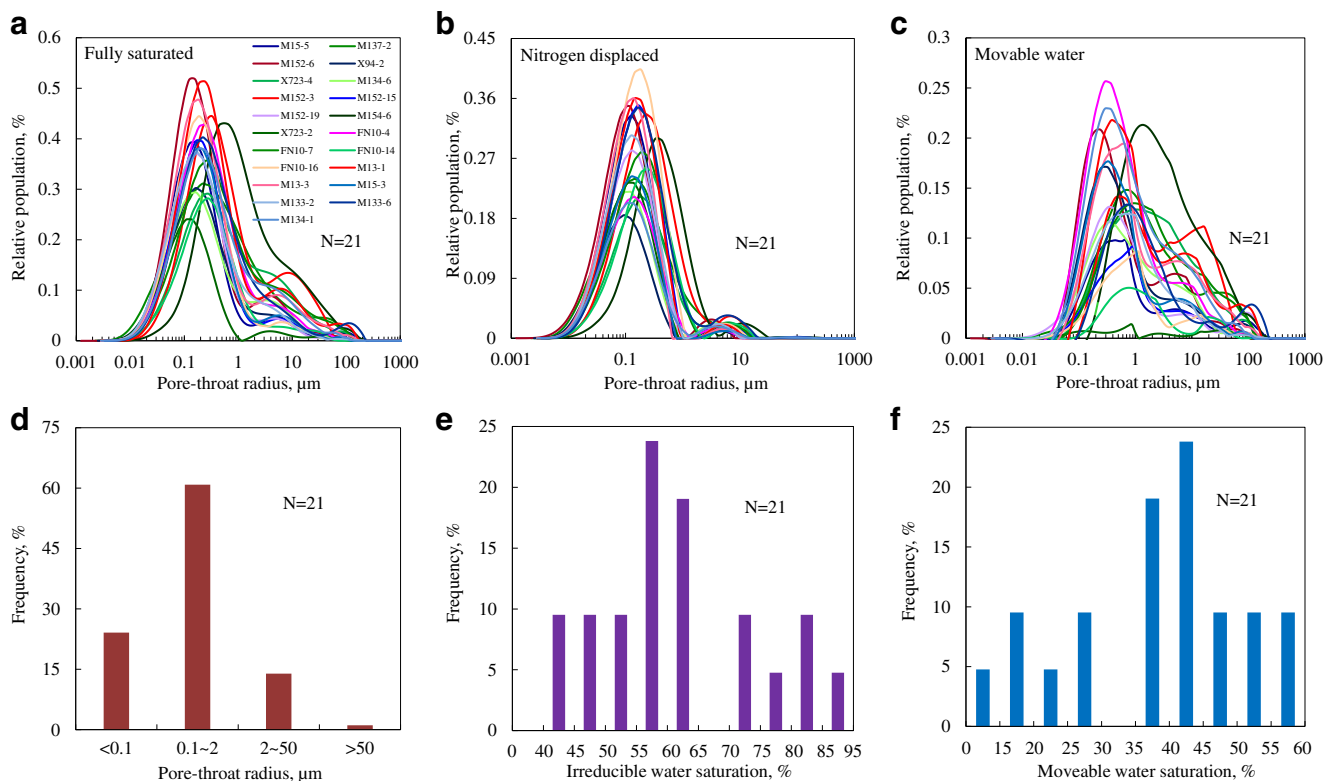


Fig. 7 a Pore-throat radius distribution from NMR of fully saturated samples. b Pore-throat radius distribution from NMR of the pore fluid displaced by nitrogen. c Pore-throat radius distribution of movable fluid from NMR.

d Frequency histogram of pore-throat interval from NMR of fully saturated samples. e Frequency histogram of bound water saturation. f Frequency histogram of movable water saturation for the 21 core samples

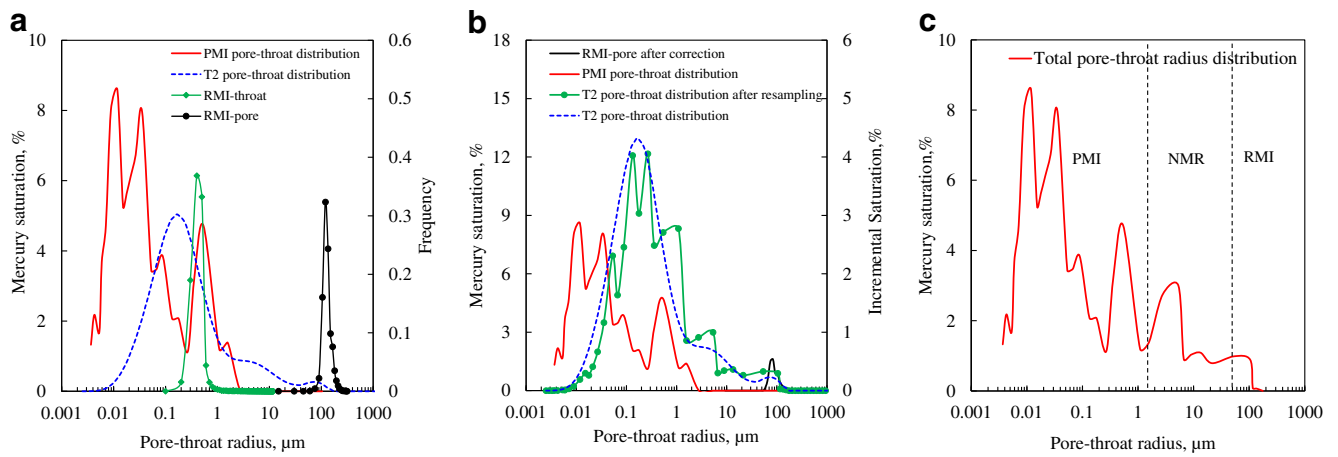


Fig. 8 Diagram of the TRD reconstruction progress—a case of sample X94-2. **a** The original pore-throat radius distribution of PMI, RMI, and fully saturated T_2 spectra. **b** Pore radius distribution of RMI after pore radius correction and volume frequency change and the pore-throat radius distribution of fully saturated T_2 spectra after resampling. **c** The final reconstructed TRD curves.

the inscribed sphere. Then, the value of the correction coefficient could be obtained, which equals 0.67, that is, the value of a in the relationship $R_0 = a R_p$.

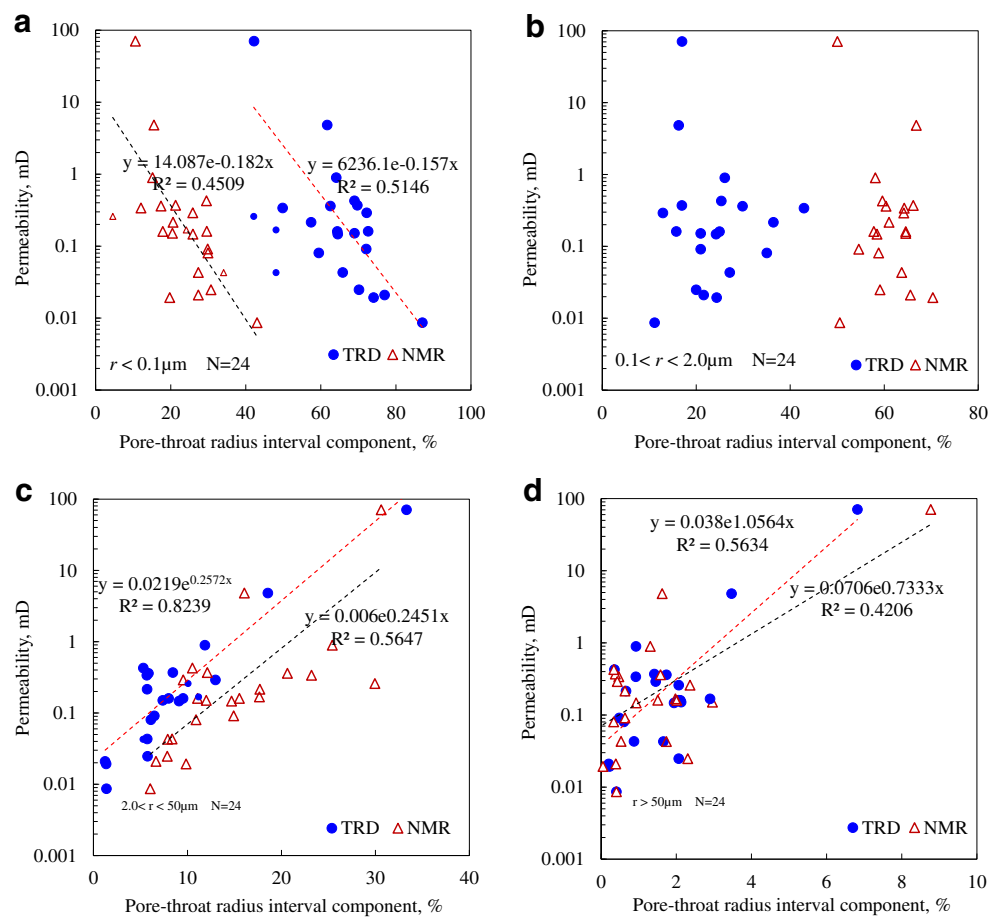
To combine the RMI and PMI (Fig. 8a), here firstly, the number frequency of pore distribution by RMI must be transformed to the volume frequency, and the pore radius also

Table 2 Characteristic parameters of TRD and the converted fully saturated NMR T_2 spectra

Sample	ϕ (%)	k (mD)	S_{wr} (%)	S_{wm} (%)	TRD (μm)				NMR (μm)			
					< 0.1	0.1~2	2~50	> 50	< 0.1	0.1~2	2~50	> 50
X723-2	3.99	0.009	93.38	6.62	87.03	11.17	1.39	0.41	42.98	50.57	6.04	0.41
FN10-14	5.14	0.019	81.19	18.81	74.05	24.37	1.35	0.23	19.72	70.37	9.86	0.05
FN10-16	8.01	0.021	80.41	19.59	76.96	21.60	1.24	0.20	27.37	65.59	6.65	0.39
M152-15	8.06	0.043	75.76	24.24	65.83	27.16	5.72	0.88	27.37	63.73	8.37	0.53
M15-5	9.00	0.043	71.78	28.22	48.04	36.13	5.27	1.66	34.09	56.27	7.91	1.74
M133-6	9.69	0.151	70.06	29.94	68.96	20.95	7.37	2.13	20.44	64.59	12.01	2.96
M133-2	8.19	0.427	64.17	35.83	68.96	25.35	5.31	0.36	29.52	59.62	10.52	0.34
M152-19	9.36	0.025	63.11	36.89	70.17	20.01	5.75	2.07	30.72	59.13	7.85	2.31
M152-3	11.45	0.340	62.22	37.78	49.80	42.94	5.68	0.92	12.05	64.29	23.19	0.47
M152-6	10.91	0.081	60.44	39.56	59.43	35.02	6.10	0.61	29.92	58.83	10.92	0.34
FN10-7	9.02	0.362	57.70	42.30	62.55	29.87	5.84	1.74	17.41	60.38	20.63	1.58
M137-2	10.14	0.168	57.68	42.32	48.04	37.13	11.18	2.90	24.15	56.22	17.65	1.98
M134-6	6.77	0.091	57.10	42.90	72.10	20.95	6.47	0.48	29.85	54.59	14.92	0.64
M13-3	10.58	0.147	56.81	43.19	64.51	24.22	9.10	1.94	25.91	58.47	14.69	0.93
M13-1	11.62	0.160	55.56	44.44	64.40	24.96	8.00	2.11	17.89	64.58	15.52	2.01
M15-3	7.92	0.292	54.55	45.45	72.21	12.91	12.98	1.45	25.85	64.16	9.55	0.43
X723-4	8.38	0.895	51.20	48.80	64.11	26.10	11.86	0.93	15.14	58.13	25.42	1.31
M154-6	10.61	0.260	49.68	50.32	42.11	45.76	10.06	2.07	4.55	63.14	29.94	2.37
X94-2	7.03	0.161	48.71	51.29	72.61	15.79	9.54	2.06	29.61	57.81	11.07	1.51
FN10-4	10.15	0.370	42.44	57.56	69.73	16.95	8.44	1.42	21.30	66.21	12.12	0.38
M134-1	10.02	0.215	41.15	58.85	57.41	36.45	5.70	0.67	20.62	61.04	17.70	0.64
M139-3	16.41	70.980	/		42.18	16.99	33.31	6.82	10.57	50.04	30.62	8.77
X94-1	6.57	0.040			70.05	14.38	13.42	2.15	22.65	68.64	7.80	0.90
FN10-23	9.82	4.820			61.69	16.28	18.55	3.48	15.50	66.82	16.05	1.63

ϕ , porosity; k , permeability; S_{wr} , bound water saturation; S_{wm} , move water saturation; TRD , percent of four pore-throat interval of TRD; NMR , percent of four pore-throat interval of the converted fully saturated NMR T_2 spectra

Fig. 9 a–d Relationships between permeability and volume percent of different pore-throat radius intervals



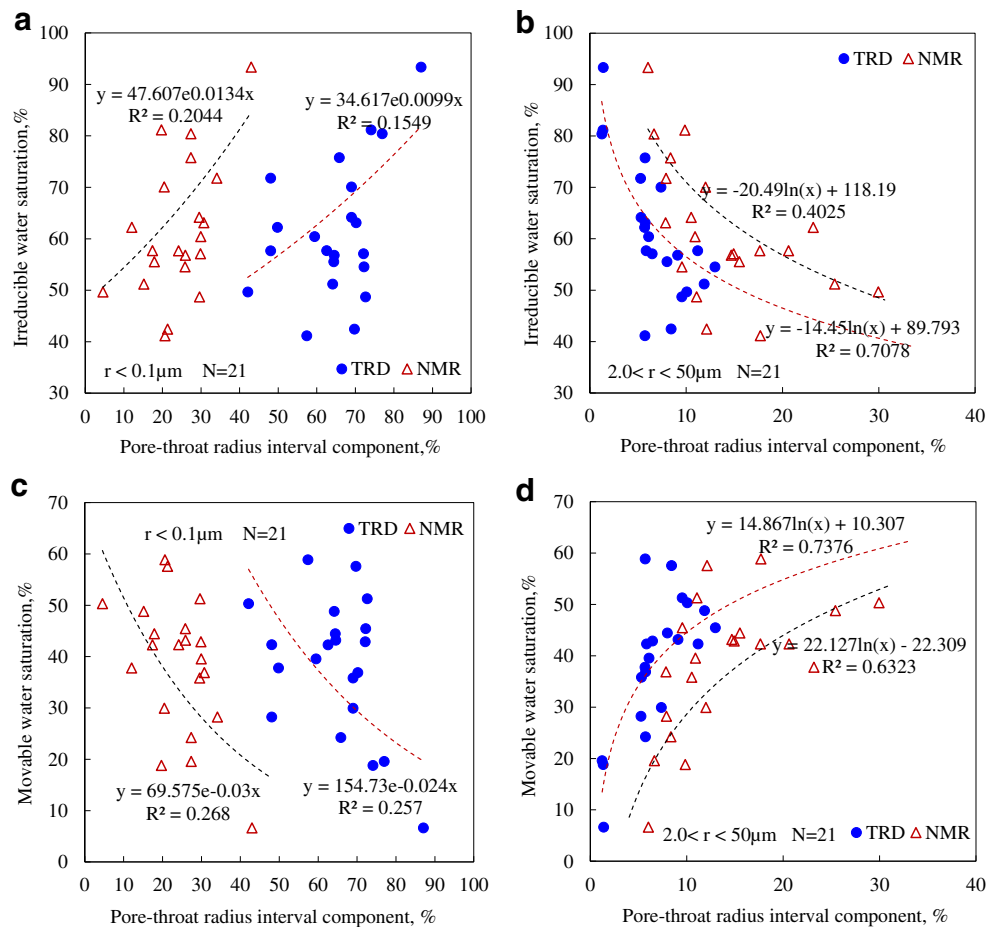
should be corrected to eliminate the effect of pores are equivalent to spheres with the same volume. Then, the pore-throat radius distribution from fully brine-saturated T_2 spectra is resampled (Fig. 8b) according to the number of samples during the PMI experiment. In Fig. 8b, the corrected pore radius distribution curves by RMI is also plotted, which shows a good consistency with the large pores from T_2 spectra of fully brine-saturated samples after resampling.

After the pore radius and volume frequency are corrected, the radius portions of the new TRD curves are reconstructed with the macropores corresponded to the corrected pore size distributions by RMI, and the missing information between PMI and RMI is reconstructed based on the pore-throat radius distribution curves of fully brine-saturated T_2 spectra after resampling. The intersection points of three types of pore-throat radius distribution curves are determined by interpolation, then, the TRD curves are reconstructed as shown in Fig. 8c. The new TRD curves retain the advantages of PMI in representing micropores and throats and the advantages of RMI in the macropores. The shortage of the missing pore-throat information between 5 and 40 μm for MIP is perfectly compensated by NMR in the new TRD curves, which means that pore-throat characteristics of the tight sandy conglomerate reservoirs could be totally represented by the new TRD curves more exactly.

Effect of pore-throat structure on physical properties and fluid distributions

Currently, there are two pore-throat classifications; the first one is defined by the International Union of Pure and Applied Chemistry (IUPAC), which was developed by Rouquerol et al. (1994). In this classification, micropores have widths less than 2 nm, mesopores range from 2 to 50 nm in width, and macropores have widths greater than 50 nm. The IUPAC pore size classification may be appropriate for chemical products, but nearly all pores and throats would be grouped with larger pores in carbonate rocks as macropores, and this is thus inadequate for reservoir systems. The second classification was developed by Loucks et al. (2012). They extended Choquette and Pray's pore size classification for carbonates and proposed a new pore size classification scheme. In this scheme, nanopores range from 1 to 1 μm , micropores range from 1 to 62.5 μm , and mesopores from 62.5 μm to 4 mm. From the results of the nitrogen-displaced NMR experiment, the bound water is mainly located in pores and throats less than 2 μm , and fluid distributed in pores larger than 50 μm is completely movable (Fig. 7b). On the basis of the pore-throat classification developed by Loucks et al. (2012), the pore-throat radius distribution of the sandy

Fig. 10 a–d Relationship between volume percent of four pore-throat interval and S_{wr} and S_{wm}



conglomerate reservoirs of the Mabei oil field can be divided into four intervals combined with the experiment results. Clay mineral pores are less than 0.1 μm in width, and the main pore type is intergranular micropores of kaolinite. Nanopores range from 0.1 to 2 μm in width; the main pore type is residual grain dissolution pores cemented by calcium in Fig. 3a. Micropores have widths between 2 and 50 μm , and the main pore types are residual intergranular pores and grain dissolution pores in Fig. 3c. Mesopores have widths greater than 50 μm , and original intergranular pores are the main pore types in Fig. 3f.

The characteristic parameters for 24 samples are listed in Table 2; it is deduced that the pore-throat structure, especially the throat radii, have a significant influence on the permeability of tight reservoirs (Figs. 3b and 5b). Relationships between permeability and volume percent of different pore-throat radius intervals are built and plotted in Fig. 9; it shows that the permeability decreases with the increase of the volume percentage for clay mineral pores (pore-throat radius $r < 0.1 \mu\text{m}$, Fig. 9a), which indicates that clay minerals will destroy the flow properties in tight sandy conglomerate reservoirs. However, the nanopores have no obvious effect on permeability as showed in Fig. 9b. While for mesopores, it seems that the higher volume percentage is corresponded to the larger permeability but with a low correlation coefficient in

Fig. 9d. For micropores, there is the best relationship between permeability and the micropore volume percentage as the correlation coefficient $R^2 = 0.8239$ in Fig. 9c. TRD curves can represent the pore-throat size distribution more precisely than the T_2 spectra of fully water-saturated samples. The permeability model is established based on the volume percentage of micropores in the TRD curves in Eq. (5) where k is the permeability in mD and P_{cr} are the volume percentages of the pores and throats between 2.0 and 50 μm , %,

$$k = 0.0219e^{0.2572P_{cr}} \tag{5}$$

The NMR experiments indicate that the pore-throat radius has a great influence on fluid distribution. Bound water saturation is higher, and movable water saturation is lower with an increased volume percentage of clay mineral pores as shown in Fig. 10a, c. The volume percentage of the micropores has the best correlation with bound water saturation and movable water saturation ($R^2 = 0.7078$, $R^2 = 0.7376$). Bound water saturation is lower and movable water saturation is higher with the increased micropore volume percentage in Fig. 10b, d. The bound water saturation is the ratio of the cumulative porosity percentage of T_2 spectra of the pore fluid displaced by

nitrogen to the cumulative porosity percentage of T_2 spectra of fully saturated samples. The movable water saturation is the ratio of the cumulative porosity percentage of T_2 spectra of the movable water to the cumulative porosity percentage of T_2 spectra of fully saturated samples. Both the bound water saturation and movable water saturation are dynamic parameters. Therefore, the volume percentage of the micropores, which can reflect the spatial correlation between the pores and throats and flow characteristics of tight reservoirs, has the best correlation with bound water and movable water saturation. TRD curves can represent the fluid distribution more precisely compared with the T_2 spectra of fully water-saturated samples, and the characteristic parameters of TRD and T_2 spectra of fully saturated samples are listed in Table 2. Therefore, the bound water saturation and movable water saturation models of the Mabei oil field are established according to the volume percentage of the micropores of the new TRD curves in Eqs. (6) and (7),

$$S_{wr} = -14.45 \ln(P_{cr}) + 89.79 \quad (6)$$

$$S_{wm} = 14.87 \cdot \ln(P_{cr}) + 10.31 \quad (7)$$

Here, S_{wr} is the bound water saturation, %; S_{wm} is the movable water saturation, %; and P_{cr} is the volume percentage of pores between 2.0 and 50.0 μm , %.

Conclusions

1. The overall pore-throat size distributions were reconstructed by combining MIP and NMR, which retained the advantages of PMI for micropores and RMI for macropores and reflected the pore-throat characteristics more precisely for tight sandy conglomerate reservoirs.
2. The bound water mainly remained in pores and throats less than 2.0 μm , corresponding to a high bound water saturation and an average value of 60%, and the fluid distributed in pores and throats larger than 50 μm is completely movable.
3. The new TRD curves are classified into nanopores, micropores, and mesopores; reservoir quality and fluid distribution mainly controlled by micropores by effecting the permeability and irreducible water distributions in tight sandy conglomerate reservoirs.

Acknowledgments The authors would like to thank the help from the Xinjiang Oilfield Company, CNPC.

Funding information This project was supported by the National Natural Science Foundation of China (No. 41804141) and the Chinese Postdoctoral Science Foundation (NO.2018M643525). And this work was also supported by the Scientific Research and Technology Development Project of CNPC (No. 2016D-3802) and the National

Key Basic Research Program of China (973 Program) (No. 2015CB250902).

References

- Chen M, Li M, Zhao JZ, Kuang Y (2018a) Irreducible water distribution from nuclear magnetic resonance and constant-rate mercury injection methods in tight oil reservoirs. *Int J Oil, Gas Coal Technol* 17(4):443–457
- Chen M, Dai JC, Liu XJ, Qin MJ, Pei Y, Wang ZT (2018b) Differences in the Fluid Characteristics between Spontaneous Imbibition and Drainage in Tight Sandstone Cores from Nuclear Magnetic Resonance. *Energy & Fuels* 32 (10):10333–10343
- Clarkson CR, Jensen JL, Blasingame TA (2011) Reservoir engineering for unconventional gas reservoirs: what do we have to consider? *SPE* 1–45
- Clarkson CR, Solano N, Bustin RM, Bustin AMM, Chalmers GRL, He L, Melnichenko YB, Radliński AP, Blach TP (2013) Pore structure characterization of North American shale gas reservoirs using USANS/SANS, gas adsorption, and mercury intrusion. *Fuel* 103(1):606–616
- Ghanizadeh A, Clarkson CR, Aquino S, Ardakani OH, Sanei H (2015) Petrophysical and geomechanical characteristics of Canadian tight oil and liquid-rich gas reservoirs: II. Geomechanical property estimation. *Fuel* 153(1):682–691
- Jorand R, Fehr A, Koch A, Clauser C (2011) Study of the variation of thermal conductivity with water saturation using nuclear magnetic resonance. *J Geophys Res Solid Earth* 116(B8):4684–4698
- Kampschulte M, Langheinrich AC, Sender J, Litzlbauer HD, Althöhn U, Schwab JD, Alejandre-Lafont E, Martels G, Krombach GA (2016) Nano-computed tomography: technique and applications. *Fortschr. Rontgenstrasse* 188(2):146–154
- Klaver J, Desbois G, Urai JL, Littke R (2012) BIB-SEM study of the pore space morphology in early mature Posidonia Shale from the Hils area, Germany. *Int J Coal Geol* 103(23):12–25
- Leng ZP, Lv WF, Ma DS, Liu QJ, Jia NH, Li T, Jin X, Li DY (2015) Characterization of pore structure in tight oil reservoir rock. *SPE* 1–8
- Loucks RG, Reed RM, Ruppel SC, Hammes U (2012) Spectrum of pore types and networks in mudrocks and a descriptive classification for matrix-related mudrock pores. *AAPG Bull* 96(6):1071–1098
- Mayo S, Josh M, Nesterets Y, Esteban L, Pervukhina M, Clennel MB, Maksimenko A, Hall C (2015) Quantitative micro-porosity characterization using synchrotron micro-CT and xenon K-edge subtraction in sandstones, carbonates, shales and coal. *Fuel* 154:167–173
- Neasham JW (1986) Applications of scanning electron microscopy to characterization and evaluation of reservoir rocks. *Am Assoc Pet Geol Bull* 70(5):15–18
- Qiao J, Zeng J, Yang Z, Feng X, Yao JL, Luo AX (2015) The Nano-macro pore network and the characteristics of petroleum migration and accumulation in Chang 8 tight sandstone reservoir in Heshui, Ordos Basin. *Acta Geol Sin (Eng Ed)* 89(S1):207–209
- Rouquerol J, Avnir D, Fairbridge CD, Everett DH, Haynes JH, Pernicone N, Ramsay JDF, Sing KSW, Unger KK (1994) Guidelines for the characterization of porous solids. *Pure Appl Chem* 66(8):1739–1758
- Schmitt M, Fernandes CP, Neto JABDC, Wolf FG, Dos Santos VSS (2013) Characterization of pore systems in seal rocks using nitrogen gas adsorption combined with mercury injection capillary pressure techniques. *Mar Pet Geol* 39(1):138–149
- Tinni A, Odusina E, Sulucarnain I, Sondergeld C, Rai CS (2015) Nuclear-magnetic-resonance response of brine, oil, and methane in organic-rich shales. *SPE Reserv Eval Eng* 18(3):400–406
- Volokitin Y, Looyestijn WJ, Slijkerman WFJ, Hofman JP (2001) A practical approach to obtain primary drainage capillary pressure curves from NMR core and log data. *Petrophysics* 42(4):334–343

- Wang C, Li T, Gao H, Zhao JS, Li HA (2017) Effect of asphaltene precipitation on CO₂-flooding performance in low-permeability sandstones: a nuclear magnetic resonance study. *RSC Adv* 7(61): 38367–38376
- Washburn EW (1921) The dynamics of capillary flow. *Phys Rev Lett* 17(3):273–283
- Xi K, Cao Y, Haile BG, Zhu RK, Jahren J, Bjørlykke K, Zhang XX, Hellevang H (2016) How does the pore-throat size control the reservoir quality and oiliness of tight sandstones? The case of the lower Cretaceous Quantou formation in the southern Songliao Basin, China. *Mar Pet Geol* 76:1–15
- Xiao L, Mao ZQ, Wang ZN, Jin Y (2012) Application of NMR logs in tight gas reservoirs for formation evaluation: a case study of Sichuan basin in China. *J Pet Sci Eng* 81(2):182–195
- Xiao DS, Lu SF, Lu ZY, Huang W, Gu MW (2016a) Combining nuclear magnetic resonance and rate-controlled porosimetry to probe the pore-throat structure of tight sandstones. *Pet Exp Dev* 43(6):1049–1059
- Xiao L, Wang H, Zou CC, Mao ZQ, Guo HP (2016b) Improvements on "Application of NMR logs in tight gas reservoirs for formation evaluation: a case study of Sichuan basin in China". *J Pet Sci Eng* 138(2):11–17
- Yao Y, Liu D (2012) Comparison of low-field NMR and mercury intrusion porosimetry in characterizing pore size distributions of coals. *Fuel* 95:152–158
- Yao YB, Liu DM, Che Y, Tang DZ, Tang SH, Huang WH (2010) Petrophysical characterization of coals by low-field nuclear magnetic resonance (NMR). *Fuel* 89(7):1371–1380
- Yuan HH (1991) Advances in apex technology: determination of cementation exponent and absolute permeability. *Log Anal* 32(5):557–570
- Yuan HH, Swanson BF (1989) Resolving pore-space characteristics by rate-controlled porosimetry. *SPE Form Eval* 4(1):17–24
- Zhao H, Ning Z, Wang Q, Zhang R, Zhao TY, Niu TF, Zeng Y (2015) Petrophysical characterization of tight oil reservoirs using pressure-controlled porosimetry combined with rate-controlled porosimetry. *Fuel* 154:233–242
- Zou CN (2017) Unconventional petroleum geology. Part III: unconventional petroleum miscellany. Chapter 9-tight oil and gas, Petroleum Industry Press, pp 239–273